



LAWRENCE
LIVERMORE
NATIONAL
LABORATORY

Energy transfer between laser beams crossing in ignition hohlraums

P. Michel, L. Divol, E. A. Williams, C. A. Thomas, D. A. Callahan, S. Weber, S. W. Haan, J. D. Salmonson, N. B. Meezan, O. L. Landen, S. Dixit, D. E. Hinkel, M. J. Edwards, B. J. MacGowan, J. D. Lindl, S. H. Glenzer, L. J. Suter

December 15, 2008

Physics of Plasmas

Disclaimer

This document was prepared as an account of work sponsored by an agency of the United States government. Neither the United States government nor Lawrence Livermore National Security, LLC, nor any of their employees makes any warranty, expressed or implied, or assumes any legal liability or responsibility for the accuracy, completeness, or usefulness of any information, apparatus, product, or process disclosed, or represents that its use would not infringe privately owned rights. Reference herein to any specific commercial product, process, or service by trade name, trademark, manufacturer, or otherwise does not necessarily constitute or imply its endorsement, recommendation, or favoring by the United States government or Lawrence Livermore National Security, LLC. The views and opinions of authors expressed herein do not necessarily state or reflect those of the United States government or Lawrence Livermore National Security, LLC, and shall not be used for advertising or product endorsement purposes.

Energy transfer between laser beams crossing in ignition hohlraums

P. Michel, L. Divol, E. A. Williams, C. A. Thomas, D. A. Callahan, S. Weber, S. W. Haan, J. D. Salmonson, N. B. Meezan, O. L. Landen, S. Dixit, D. E. Hinkel, M. J. Edwards, B. J. MacGowan, J. D. Lindl, S. H. Glenzer, and L. J. Suter
Lawrence Livermore National Laboratory, Livermore, CA 94551

The full scale modeling of power transfer between laser beams crossing in plasmas is presented. A new model was developed, allowing calculations of the propagation and coupling of pairs of laser beams with their associated plasma wave in three dimensions. The complete set of laser beam smoothing techniques used in ignition experiments are modeled, and their effects on crossed-beam energy transfer is investigated. A shift in wavelength between the beams can move the instability in or out of resonance and hence allows tuning of the energy transfer. The effects of energy transfer on the effective beam pointing and on symmetry have been investigated. Several ignition designs have been analyzed and compared, indicating that a wavelength shift of up to 2 Å between cones of beams should be sufficient to control energy transfer in ignition experiments.

I. INTRODUCTION

Energy transfer between laser beams crossing in a plasma is a topic of very high importance for indirect-drive ignition experiments [1–4] due to its impact on the implosion symmetry of the fuel capsule [5–16]. In this process, described as *induced* Brillouin scattering in Ref. [5], the beat wave generated by the interference pattern of two laser beams crossing at a half-angle ϕ_s resonantly excites an ion acoustic wave (IAW) that can in turn transfer energy from one beam to the other. The process becomes resonant when the IAW dispersion relation is satisfied: $\omega_0 - \omega_1 = |\mathbf{k}_0 - \mathbf{k}_1|c_s + (\mathbf{k}_0 - \mathbf{k}_1) \cdot \mathbf{V}$, where ω_0, ω_1 and $\mathbf{k}_0, \mathbf{k}_1$ are the respective frequencies and wavenumbers of the two laser beams, c_s is the ion acoustic velocity and \mathbf{V} is the plasma flow. Energy transfer can occur if both laser beams have the same wavelength in presence of a Mach 1 flow ($V \simeq c_s$) aligned with $\Delta \mathbf{k} \equiv \mathbf{k}_0 - \mathbf{k}_1$. In turn, introducing a wavelength shift between the beams (i.e. setting $\Delta \omega \equiv \omega_0 - \omega_1 \neq 0$) detunes the process away from resonance (cf. Fig. 1).

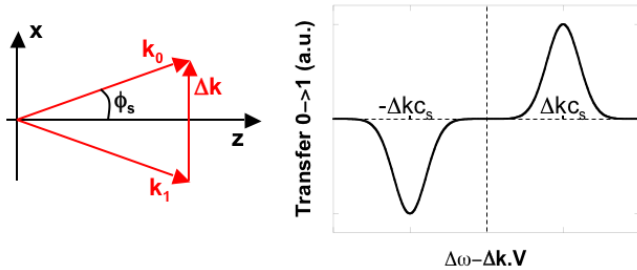


FIG. 1: \mathbf{k} -vector diagram for the crossed-beam energy transfer process.

Previous theoretical studies [5, 13, 14] showed that the flow at the laser entrance hole (LEH) of ignition hohlraums resembles that of a supersonic nozzle with the plasma transitioning through Mach one in the throat and becoming supersonic outside. These conditions can allow for induced Brillouin scattering between beams at

the same wavelength. The ability to induce a wavelength shift between the beams was therefore suggested and implemented on the National Ignition Facility (NIF) in order to detune the instability and reduce the transfer, based upon one-dimensional (1D) ray-based analysis [14].

In this paper, we present the first full scale, three dimensional numerical modeling of crossed beam energy transfer in ignition hohlraums with realistic laser and plasma conditions. Our model calculates the propagation and coupling of two laser beams and of the IAW excited by their beat wave. The lasers are modeled with a steady-state paraxial model, and the plasma wave is described by a linear kinetic model. The laser fields include realistic electric field profiles measured from the NIF laser with continuous phase plates (CPP) and polarization smoothing (PS). Smoothing by spectral dispersion (SSD) is also included through a convolution of the ion wave response with the laser bandwidth. The amplitude of the IAW is monitored and remains very small in ignition conditions, justifying a linear model for the plasma wave. This model therefore provides quantitative estimates for the energy transfer between the two laser beams in a full scale hohlraum.

The model is presented in Sec. II. Sec. III presents results for one particular pair of beams; in particular, we show that a wavelength shift between the beams allows control of the energy transfer by shifting the plasma wave resonance conditions. We discuss the effects of the laser beam smoothing techniques on crossed-beam energy transfer. In Sec. IV, the study is extended to the full NIF; we calculate the global energy gain for each beam by summing up the contributions from each of its neighboring beams. We investigate the effects of the energy transfer on the spatial profiles of the beams, and show that the transfer leads to a systematic pointing shift towards the LEH. The results of our model are finally used with a view factor code that calculates the effects of crossed-beam transfer on the capsule implosion symmetry. Sec. V summarizes our results.

II. DESCRIPTION OF THE MODEL

We have developed a new 3D model that calculates the steady-state propagation and coupling of a system of two crossing laser beams $\mathbf{a}_0, \mathbf{a}_1$ (the total normalized vector potential is $\mathbf{a} = \mathbf{a}_0 + \mathbf{a}_1$, with $\mathbf{a} = e\mathbf{A}/mc^2$ where \mathbf{A} is the vector potential) and the IAW excited by their beat wave. The IAW electron density perturbation is noted δn_a . We use the following enveloped expression for the three waves:

$$\begin{aligned} \mathbf{a}_0 &= \frac{1}{2} (\hat{a}_{0x} e^{i\phi_0} + c.c.) \mathbf{x}_0 + \frac{1}{2} (\hat{a}_{0y} e^{i\phi_0} + c.c.) \mathbf{y}_0 \quad (1) \\ \mathbf{a}_1 &= \frac{1}{2} (\hat{a}_{1x} e^{i\phi_1} + c.c.) \mathbf{x}_1 + \frac{1}{2} (\hat{a}_{1y} e^{i\phi_1} + c.c.) \mathbf{y}_1 \quad (2) \\ \delta n_a &= \frac{1}{2} (\delta \hat{n}_a e^{i\phi_a} + c.c.). \quad (3) \end{aligned}$$

The polarizations directions are similar to the ones used for the PS scheme on NIF; each beam has half of its power polarized along the polar direction (\mathbf{x}_0 and \mathbf{x}_1) and the other half polarized along the azimuthal direction (\mathbf{y}_0 and \mathbf{y}_1), as represented in Fig. 2. The phases are $\phi_0 = k_0(z)z \cos(\phi_s) + k_0(z)x \sin(\phi_s) - \omega_0 t$ and $\phi_1 = k_0(z)z \cos(\phi_s) - k_0(z)x \sin(\phi_s) - \omega_1 t$. We will allow for a small wavelength separation between the beams, however this will be small enough to neglect its effects on the propagation of the beams (cf. next section). Therefore, we choose the same envelope wavenumber for both beams, weighted in the transverse direction by the intensity in the same manner as Ref. [17]: $k_0(z) = (\omega_0/c) \sqrt{1 - n_0(z)/n_c}$ with $n_0(z) = \langle |\mathbf{a}|^2(x, y, z) n_e(x, y, z) \rangle_{\perp} / \langle |\mathbf{a}|^2(x, y, z) \rangle_{\perp}$ (the brackets denote a spatial average over the transverse directions (x, y)). In order to minimize the error from the paraxial approximation, the simulation box is chosen so that its z axis bisects $(\mathbf{k}_0, \mathbf{k}_1)$. The x axis lies in the plane $(\mathbf{k}_0, \mathbf{k}_1)$. Phase matching conditions are assumed between the three waves, i.e. $\phi_a = \Delta \mathbf{k} \cdot \mathbf{x} - \Delta \omega t \equiv \phi_0 - \phi_1$.

The IAW is described in the linear kinetic limit. The linearized Vlasov equation coupled to Poisson's equation lead to the following expression for the ion acoustic wave density perturbation [18]:

$$\delta \hat{n}_a = \frac{\chi_e(1 + \chi_i)}{1 + \chi_e + \chi_i} \frac{ik_p \hat{F}_p}{4\pi e^2}, \quad (4)$$

where χ_e and χ_i are the electron and ion susceptibilities and \hat{F}_p is the component of the ponderomotive force oscillating at ϕ_a , i.e. $\mathbf{F}_p = \frac{1}{2} \{ \hat{F}_p \exp[i\phi_a] + c.c. \}$.

Since $\mathbf{F}_p = -\frac{1}{2} mc^2 \nabla \mathbf{a}^2$, we get:

$$\hat{F}_p = -\frac{1}{2} ik_p mc^2 X, \quad (5)$$

$$\begin{aligned} X &\equiv \hat{a}_{0x} \hat{a}_{1x}^* \mathbf{x}_0 \cdot \mathbf{x}_1 + \hat{a}_{0x} \hat{a}_{1y}^* \mathbf{x}_0 \cdot \mathbf{y}_1 \\ &\quad + \hat{a}_{0y} \hat{a}_{1x}^* \mathbf{y}_0 \cdot \mathbf{x}_1 + \hat{a}_{0y} \hat{a}_{1y}^* \mathbf{y}_0 \cdot \mathbf{y}_1. \end{aligned} \quad (6)$$

Deriving a set of coupled paraxial equations for the four laser fields components (two polarizations per beam)

leads to:

$$\mathcal{P} \begin{pmatrix} \hat{a}_{0x} \\ \hat{a}_{0y} \\ \hat{a}_{1x} \\ \hat{a}_{1y} \end{pmatrix} = -\frac{i\omega_{p0}^2}{4k_0 c^2 n_0} \begin{pmatrix} \delta \hat{n}_a \hat{a}_{1x} \\ \delta \hat{n}_a \hat{a}_{1y} \\ \delta \hat{n}_a^* \hat{a}_{0x} \\ \delta \hat{n}_a^* \hat{a}_{0y} \end{pmatrix} \quad (7)$$

where $\mathcal{P} = \left(\partial_z - \frac{i\nabla_{\perp}^2}{k_0 + \sqrt{k_0^2 + \nabla_{\perp}^2}} + \frac{k'_0}{2k_0} + \frac{i\omega_{p0}^2 \delta n_h}{2k_0 c^2 n_0} + \frac{\nu_{ei} \omega_{p0}^2}{2\omega_0 k_0 c^2} \right)$. Here $k'_0(z) = dk_0/dz$, $\delta n_h = n_e(x, y, z) - n_0(z)$ is the transverse density variation, ν_{ei} is the electron-ion collision frequency and $\omega_{p0}^2 = 4\pi e^2 n_0/m_e$ is the plasma frequency. The first two terms of the propagator \mathcal{P} describe the propagation and diffraction with modified paraxial conditions [17]; the third term is the swelling factor (ensuring energy flux conservation), and the fourth and fifth terms represent the refraction on inhomogeneous density profiles and the inverse Bremsstrahlung absorption.

Replacing the expressions for $\delta \hat{n}_a$ in these equations leads to the following system of four coupled paraxial equations:

$$\mathcal{P} \begin{pmatrix} \hat{a}_{0x} \\ \hat{a}_{0y} \end{pmatrix} = -i\gamma X \begin{pmatrix} \hat{a}_{1x} \\ \hat{a}_{1y} \end{pmatrix} \quad (8)$$

$$\mathcal{P} \begin{pmatrix} \hat{a}_{1x} \\ \hat{a}_{1y} \end{pmatrix} = -i\gamma^* X^* \begin{pmatrix} \hat{a}_{0x} \\ \hat{a}_{0y} \end{pmatrix} \quad (9)$$

Each of these four equations is solved by integrating the fields over one numerical step δz using operator splitting. Each operator in \mathcal{P} is solved analytically by integrating from z to $z + \delta z$ (the diffraction step is done in Fourier space), except for the coupling step which uses a second order finite difference scheme.

The coupling term $\gamma(\mathbf{k}, \omega) = (\Delta k/8k_0) \chi_e(1 + \chi_i)/(1 + \chi_e + \chi_i)$ is calculated at $(\mathbf{k}, \omega - \mathbf{kV})$ where \mathbf{V} is the plasma flow. This coupling term has been modified to account for both the spatial frequency broadening due to the finite aperture of the optics in near-field, and the time frequency broadening induced by the smoothing by spectral dispersion (SSD). These effects can smooth out the effects of local sharp resonances in the plasma. Indeed, each point in the far-field is illuminated by a range of wave-vectors spread over the beam's near field and by a range of frequencies spread over the SSD bandwidth (cf. Fig.2).

Averaged over a SSD modulator period, the time and space frequencies can be considered independent. A SSD phase modulation of the form $\exp[-i\delta \sin(\Omega_m t)]$ in the near field gives a far-field spectral density $I_{\omega} = \sum_{-\infty}^{+\infty} J_n^2(\delta) \delta(\omega - n\Omega_m)$. The average coupling coefficient is thus calculated by a double discrete sum (over the SSD δ -peaks) of a quadruple integral (over the lenses' \mathbf{k} -vectors) of the local coefficient γ :

$$\begin{aligned} \bar{\gamma} &= \sum_{l, l' = -\infty}^{+\infty} \iint \mathcal{A}_1(\mathbf{k}'_{\perp} - \Delta \mathbf{k}/2) \mathcal{A}_0(\mathbf{k}''_{\perp} + \Delta \mathbf{k}/2) \\ &\quad J_l^2(\delta) J_{l'}^2(\delta) \gamma(\mathbf{k}'_{\perp} - \mathbf{k}''_{\perp}, \Delta \omega + (l - l')\Omega_m) d\mathbf{k}'_{\perp} d\mathbf{k}''_{\perp} \quad (10) \end{aligned}$$

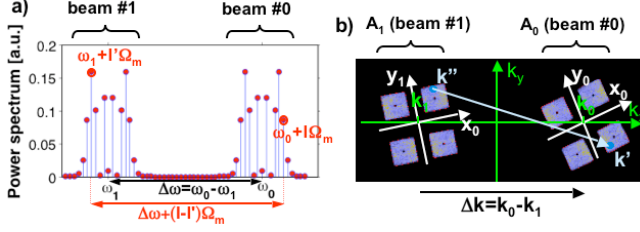


FIG. 2: Frequency broadening of the effective frequency and wave vector of the laser: a) in the time domain, due to SSD; b) in the spatial domain, due to the optics finite aperture (represented is the near-field of two NIF beams). Our coupling coefficient is averaging over all possible weighted pairs of frequencies and wave vectors (Eq. (10))

where $\mathcal{A}_0, \mathcal{A}_1$ are the intensity distribution of the laser beams in the near field normalized such as $\int \mathcal{A}_{0,1}(\mathbf{k}_\perp) d\mathbf{k}_\perp = 1$.

Note that the decomposition of the fields into two polarizations, Eq.(3), naturally allows for a description of polarization smoothing (PS). We use the electric fields measured from NIF, that include the phase from continuous phase plates and aberrations. All the beam smoothing techniques used in ignition experiments are thus included in our code. The hydrodynamic profiles are provided from the radiative hydrodynamic codes LASNEX [19] or HYDRA [20].

III. ENERGY TRANSFER BETWEEN ONE PAIR OF BEAMS: 30° AND 50°

A. Coupling geometry

Our model was applied to the latest NIF target design at this date (“Rev2”, with a radiation temperature of 285 eV and a Be ablator). LASNEX simulations provide the full hydrodynamics conditions required for the calculation of the propagation and coupling of the laser and plasma waves. As an example, Fig. 3 shows the material composition, electron density and temperature; at the hohlraum LEH, where the beams cross and can transfer energy, the typical conditions are $n_e/n_c \simeq 6\%$, $T_e \simeq 5\text{--}6$ keV, in a CH plasma. The 2D cylindrical data from LASNEX are interpolated onto the 3D cartesian mesh of our code.

The 192 laser beams on NIF are gathered into 48 quadruplets of beams or “quads”; 4 quads at 23.5°, 4 at 30°, 8 at 44.5° and 8 at 50° enter each LEH. The properties of the quads for that particular ignition target design are summarized on Table I. The spot sizes are defined as the semi-major and semi-minor axes a and b of the 50% intensity contour ellipse (the minor axis of a beam is in its polar plane in order to fit the ellipse into the circular LEH). In the remaining of the paper, we will refer to the quads as “beams” (e.g. the 30° beam refers to

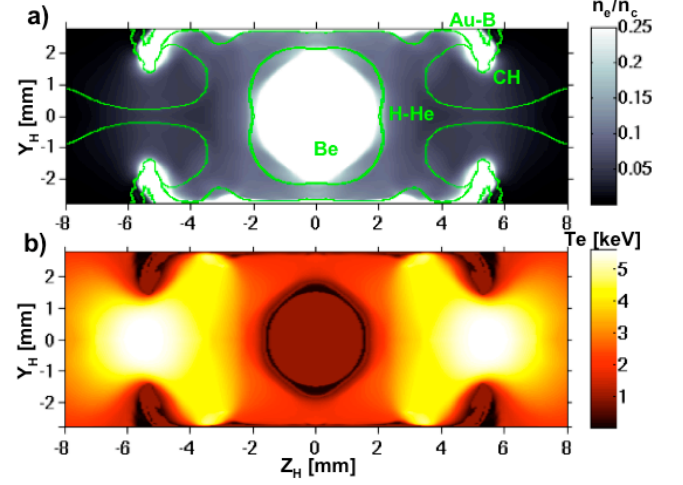


FIG. 3: Hydrodynamic conditions in NIF hohlraums at peak laser power from LASNEX simulations: a) Electron density and material composition; b) Electron temperature.

the 30° quad etc.), and to the individual beams within a quad as “beamlets”.

θ [°]	$a \times b$ [mm ²]	P [TW]	I_{14}
23.5, 30	0.968×0.693	7.97	3.8
44.5, 50	0.697×0.403	7.68	8.7

TABLE I: NIF laser parameters used for the “285 eV Be” design, per quad: polar angle θ , spot dimensions at best focus a and b , power P and average intensity I_{14} in units of 10^{14} W/cm^2 .

We start with an investigation of the coupling for one particular pair of beams (at 30° and 50° from the hohlraum axis). Figure 4a shows the hohlraum electron density with the flow (black arrows) and the rectangle box represents the simulation box. Fig. 4b shows the laser intensity for the 30° and 50° beams in the $(x, y = 0, z)$ plane (the beams \mathbf{k} -vectors are in the (x, z) plane, and have z as their bisector).

The coupling for small $\delta\lambda = \lambda_0 - \lambda_1$ values (where λ_0 and λ_1 are the wavelengths of the 30° and 50° beams) occurs mainly in two regions, just outside and just inside of the LEH. The expanding CH liner that originally covers the hohlraum lips produces a flow that is directed towards $x > 0$ near $z \simeq -1.5$ mm and towards $x < 0$ near $z \simeq 1$ mm. Figure 5a shows the coupling coefficient for a wavelength shift $\delta\lambda = 1.3 \text{ \AA}$, with a vector plot of the flow; the dashed rhombus represents the zone where the laser beams cross, similar to Fig. 4. This shows that the energy transfer first occurs from the 30° towards the 50° beams (i.e. $\text{Im}[\gamma] > 0$) near $z \simeq -1.5$ mm, where \mathbf{V} is aligned with $-\Delta\mathbf{k}$, and then from the 50° to the 30° near $z \simeq +1$ mm, where \mathbf{V} is aligned with $+\Delta\mathbf{k}$.

Figure 5b represents the coupling coefficient at $x = 0$

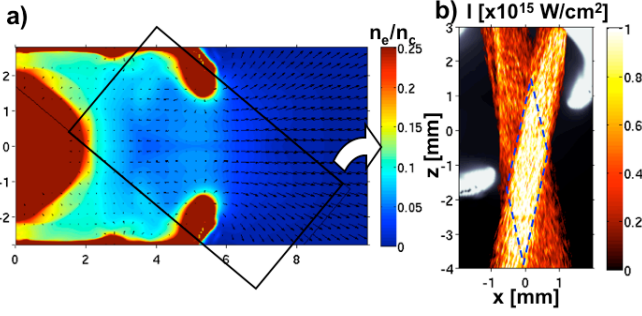


FIG. 4: a) Contour plot of a half NIF hohlraum's electron density, and flow velocity vector plot (black arrows). The black rectangle shows the location of the simulation box for the $(30^\circ, 50^\circ)$ pair of beams. b) Laser intensity in the $(x, y = 0, z)$ plane. The dashed rhombus represents the crossing area between the two beams.

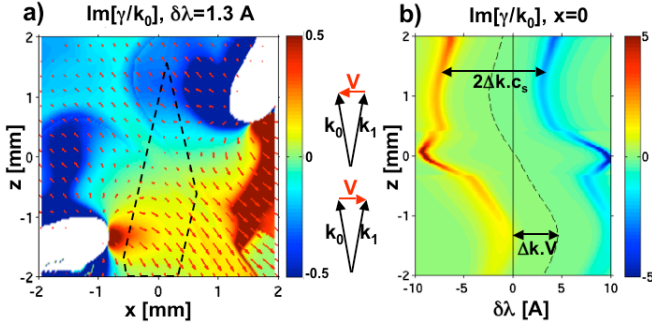


FIG. 5: a) Map of the coupling coefficient in the $(x, y = 0, z)$ simulation plane with the flow vector plot (red arrows) for the $(30^\circ, 50^\circ)$ pair of beams and $\delta\lambda = 1.3 \text{ \AA}$; the dashed rhombus represents the crossing area between the two beams. b) Coupling coefficient along the z axis (bisector line between \mathbf{k}_0 and \mathbf{k}_1) as a function of $\delta\lambda$.

(i.e. along the z axis of the simulation box) as a function of $\delta\lambda$. The $\pm\Delta k c_s$ resonances are Doppler shifted by $\Delta\mathbf{k} \cdot \mathbf{V}$, bringing the $\text{Im}[\gamma] > 0$ (resp. $\text{Im}[\gamma] < 0$) resonance peak closer to the $\delta\lambda \simeq 0$ region for $z \simeq -1.5 \text{ mm}$ (resp. $+1 \text{ mm}$), and hence transferring power from the 30° towards the 50° beam (resp. 50° towards 30°). This figure also suggests that a shift of $\delta\lambda \simeq 1.3 \text{ \AA}$ could avoid both resonances. Note that the discontinuity of $\text{Im}[\gamma]$ near $|z| \simeq 0.3 \text{ mm}$ comes from a change in material (CH liner for $|z| > 0.3 \text{ mm}$, and H-He gas mixture initially filling the hohlraum for $|z| < 0.3 \text{ mm}$).

B. Effects of laser beam smoothing

Figure 6 shows the results of our code on power transfer between the two beams as a function of $\delta\lambda$. As the gain plot from Fig. 5b already suggested, the wavelength shift that minimizes power transfer is about 1.3 \AA . The trans-

fer without frequency shift between the beams is larger than 13% regardless of the smoothing option used, due to the long propagation distances over which the coupling takes place. Note that the “zero transfer” point on Fig. 6 occurs when the positive and negative contributions from the two transfer zones exactly balance each other (the two successive and opposite transfers typically being of several percent).

The IAW amplitudes remain very small under NIF conditions (typically, we calculated the maximum $\delta n_A/n_0 \simeq 10^{-4}$, which justifies neglecting the non-linearity of the IAW [14]). Side bands are negligible as long as the first diffraction mode on the phase grating created by the beat wave of the beams is not depleted [21]. Here, the small relative energy gains (at most, $\simeq \pm 10\text{-}20\%$) allow us to neglect side bands, which also justifies using a paraxial approximation (unlike for extreme nonlinear cases where $\delta n_A/n_c \simeq 1$, and where sidebands appear at large k values, requiring non-paraxial treatment like in Ref. [6]).

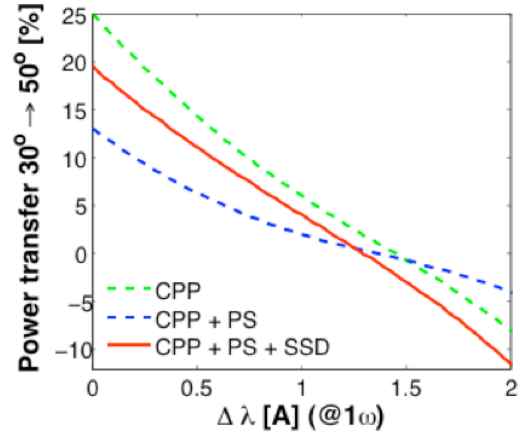


FIG. 6: Power transfer from the 30° to the 50° beams, defined as the relative power gain ΔP_{50} of the 50° beam ($\simeq -\Delta P_{30}$ since both beams have roughly the same power), with continuous phase plates (CPP) only (dashed green), CPP with PS (dashed blue), and CPP with PS and SSD (red).

Figure 6 also shows the effects of laser beam smoothing techniques available on the NIF. Polarization smoothing (PS) consists in distributing the power between two uncorrelated CPP fields at orthogonal polarizations; on NIF, the beams are grouped into quadruplets (as shown on Fig. 7a), where two beamlets are linearly polarized along the polar axis and the two others along the azimuthal axis. PS reduces the coupling by a factor two, which can be explained as follows.

Let us consider the simpler situation of two beams with aligned polarizations, i.e. $\mathbf{x}_0 \cdot \mathbf{y}_1 = \mathbf{x}_1 \cdot \mathbf{y}_0 = 0$ and $\mathbf{x}_0 \cdot \mathbf{x}_1 = \mathbf{y}_0 \cdot \mathbf{y}_1 = 1$. We will assume that the fields are given by a random phase plate (RPP) model similar to

Ref. [22]:

$$\begin{aligned}\hat{a}_{0x,y} &= \sqrt{\frac{I_{0x,y}}{N}} \sum_{\mathbf{k}_\perp \in R_0} \exp[i\mathbf{k}_\perp \cdot \mathbf{x}_\perp + i\phi^{x,y}(\mathbf{k}_\perp)] \\ \hat{a}_{1x,y} &= \sqrt{\frac{I_{1x,y}}{N}} \sum_{\mathbf{k}_\perp \in R_1} \exp[i\mathbf{k}_\perp \cdot \mathbf{x}_\perp + i\psi^{x,y}(\mathbf{k}_\perp)]\end{aligned}\quad (11)$$

where the summation is taken over the N spectral modes of the RPP in their respective domains R_0 and R_1 for the beams 0 and 1, and the random phases ϕ^x , ϕ^y , ψ^x and ψ^y are all independent (i.e. the fields at orthogonal polarizations are uncorrelated). The fields are normalized so that $\int d\mathbf{x}_\perp |\hat{a}_{0x}|^2 = P_{0x}$. For simplicity, we assume that $P_{0x} = P_{0y} = P_0/2$ and $P_{1x} = P_{1y} = P_1/2$. As we shall see, the PS effect is a purely transverse effect (i.e. the correlation of the fields in z does not matter), so we need only the coupling step in Eq. (8). We investigate the transfer for \hat{a}_{0x} , assuming that the gains are small (i.e. $e^g \simeq 1 + g$), so that we can neglect the correlation between a_0 and a_1 and depletion of a_1 . Neglecting diffraction, absorption, SSD and spatial frequency broadening effects (i.e. using γ instead of $\bar{\gamma}$), and assuming that γ is spatially uniform lead to:

$$\partial_z \hat{a}_{0x} = -i\gamma(\hat{a}_{0x}\hat{a}_{1x}^* + \hat{a}_{0y}\hat{a}_{1y}^*)\hat{a}_{1x} \quad (12)$$

We assume that an integration over a small step δz can be approximated by a finite difference; thus, multiplying the development of Eq. (12) by its complex conjugate leads to the following expression for the intensity $I_{0x} \equiv |\hat{a}_{0x}|^2$:

$$I_{0x}(z + \delta z) \simeq (1 + 2\text{Im}[\gamma]\delta z I_{1x})I_{0x}(z) + 2\delta z \text{Re}\{i\gamma^* \hat{a}_{0x}\hat{a}_{0y}^* \hat{a}_{1x}^* \hat{a}_{1y}\} + \mathcal{O}(|\gamma|^2 \delta z^2 I_{1x}^2). \quad (13)$$

In the remaining we neglect the terms which are second order in gain. We now integrate over the transverse dimensions to get the power:

$$P_{0x}(z + \delta z) = (1 + g)P_{0x}(z) + i\delta z \gamma^* \int_S d^2 \mathbf{x}_\perp \hat{a}_{0x}\hat{a}_{0y}^* \hat{a}_{1x}^* \hat{a}_{1y} + c.c. \quad (14)$$

where $g = \delta z P_1 \text{Im}[\gamma]$ and the integral is done over the surface of the beam S (such that $I_0 = S/P_0$). The second term on the RHS can be developed and simplified using the definitions of the RPP fields; we get:

$$\int d^2 \mathbf{x}_\perp \hat{a}_{0x}\hat{a}_{0y}^* \hat{a}_{1x}^* \hat{a}_{1y} = \frac{I_0 I_1}{4N^2} \sum_{\mathbf{k}_\perp, \mathbf{k}'_\perp \in R_0} \sum_{\mathbf{k}''_\perp, \mathbf{k}'''_\perp \in R_1} e^{i[\phi^x(\mathbf{k}_\perp) - \phi^y(\mathbf{k}'_\perp) - \phi^x(\mathbf{k}''_\perp) + \phi^y(\mathbf{k}'''_\perp)]} \int d^2 \mathbf{x}_\perp e^{i[\mathbf{k}_\perp - \mathbf{k}'_\perp - \mathbf{k}''_\perp + \mathbf{k}'''_\perp] \cdot \mathbf{x}_\perp} \quad (15)$$

For a given set of $(\mathbf{k}_\perp, \mathbf{k}'_\perp, \mathbf{k}''_\perp)$, there exist at most one \mathbf{k}'''_\perp for which $\mathbf{k}_\perp - \mathbf{k}'_\perp - \mathbf{k}''_\perp + \mathbf{k}'''_\perp = 0$. Therefore, the quadruple sum can be reduced to a triple sum, and since the phases are random and uncorrelated, the term scales like $\sqrt{N^3}/N^2$ and vanishes for $N \gg 1$. We are thus left with $P_{0x}(z + \delta z) = (1 + g)P_{0x}(z)$ and likewise, $P_{0y}(z + \delta z) = (1 + g)P_{0y}(z)$. Hence, since $P_0 = P_{0x} + P_{0y}$, we finally get:

$$P_0(z + \delta z) = (1 + g)P_0(z). \quad (16)$$

Now if PS is removed, e.g. by setting $\hat{a}_{0y} = \hat{a}_{1y} = 0$, we have:

$$I_0(z + \delta z) = (1 + 2\text{Im}[\gamma]\delta z I_1)I_0(z), \quad (17)$$

and hence,

$$P_0(z + \delta z) = (1 + 2g)P_0(z). \quad (18)$$

Removing PS leads to a transfer increase by a factor 2. The effect of PS is therefore different for crossed beam energy transfer compared to backscattering and/or filamentation instabilities. For the case of backscattering,

PS reduces reflectivities due to the contrast reduction of the speckle pattern [23] (except in the small gain per speckle length regime; cf. [24]). On the other hand, for crossed-beam transfer, PS reduces the transfer because of the phase-mixing of the fields components having orthogonal polarizations; this can be intuitively seen from Eq. (12), where the term \hat{a}_{1x} couples to both one term to which it is correlated (containing \hat{a}_{1x}^*), and one term to which it is not.

Figure 6 also shows that adding SSD increases the transfer values (i.e. the slopes of the curves of transfer vs. $\delta\lambda$). For $\delta\lambda \simeq 0$, the coupling originates outside the resonance of the two transfer zones. An increased laser bandwidth adds contribution from the higher coupling regions of the transfer spectrum, therefore increasing the total transfer values. In our simulation, we have used 2.2 Å of SSD bandwidth (defined at the fundamental wavelength of 1.054 μm , before the lasers frequency tripling) and a modulator frequency of 17 GHz (the modulation amplitude $\delta=5.25$). The total ± 2.2 Å bandwidth then overlaps with the resonance peaks from both zones, as represented by the grey zone on Fig. 4b, hence increasing the transfer as previously speculated in Ref. [11].

IV. ENERGY TRANSFER BETWEEN CONES OF BEAMS ON NIF

A. Average energy transfer

In order to have a description of the full effects of the transfer between beams on ignition experiments, we have calculated the coupling for all the relevant pairs of beams. All the beam lenses entering one NIF hohlraum LEH are represented on Fig. 7a. NIF has a total of 192 beamlets, grouped in “quads” (quadruplets of beamlets) at four different angles from the hohlraum axis. The 23.5° and 30° beams define the “inner cone”, which contains 8 quads at the same wavelength λ_0 , while the 44.5° and 50° beams define the “outer cone”, with 16 quads at the wavelength $\lambda_1 = \lambda_0 - \Delta\lambda$ which can be blue-shifted in the range $\Delta\lambda=[0-3]$ Å on NIF.

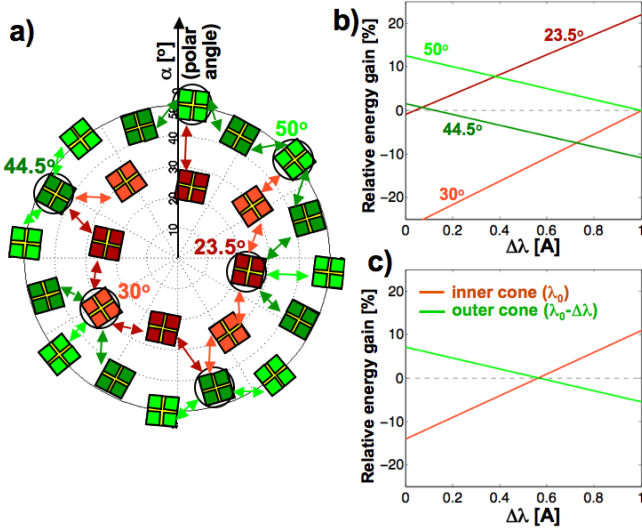


FIG. 7: a) Near-field diagram of all the beams entering one LEH of a NIF hohlraum. The total transfer for each circled beam is the sum of the contributions from all its nearest neighbors represented by the arrows (each circle represents one of the six possible nearest neighbors configurations). b) Relative energy gain per beam as a function of $\Delta\lambda$; c) relative energy gain for the inner and outer cones.

We have calculated the total transfer for each beam by summing up the contributions from all its nearest neighbors (i.e. one simulation per arrow on Fig. 7a). This remains valid as long as the transfer is not too large (second order effects were not taken into account). Note that all the pairs of beams considered here always have a half-angle separation smaller than 14° , which keeps the paraxial treatment valid. We performed gain calculations which showed that other pairs of beams are expected to have almost no transfer due to small $\Delta\mathbf{k} \cdot \mathbf{V}$ (in particular, the pairs shifted in azimuth have negligible transfers since the flow has nearly no azimuthal component). As represented in Fig. 7b, the total power transfer between

the inner and outer cones balances to zero for a wavelength shift $\delta\lambda \simeq 0.6$ Å.

B. Effects of the crossed-beam transfer on beam pointing

Another effect of the transfer is to distort the transverse intensity profile of the laser beams. This can result in a shift in the effective pointing of the beams. Figure 8a represents the transverse intensity profile of the $(30^\circ, 50^\circ)$ pair inside the hohlraum, at $z = 2$ mm (as previously defined in Fig. 4). The green crosses mark the position of the intensity-weighted center of the beam when no coupling is applied in the code; the center is defined as $\bar{x} = \langle xI(x,y) \rangle / \langle I(x,y) \rangle$ where the brackets denote a spatial average in the transverse (x,y) directions, and $\bar{y} = \langle yI(x,y) \rangle / \langle I(x,y) \rangle$. The magenta crosses represent the centers of the beams when 3 Å of wavelength shift is applied between the beams. The transfer leads to a shift of the center “upwards” (i.e. towards the LEH) for both beams.

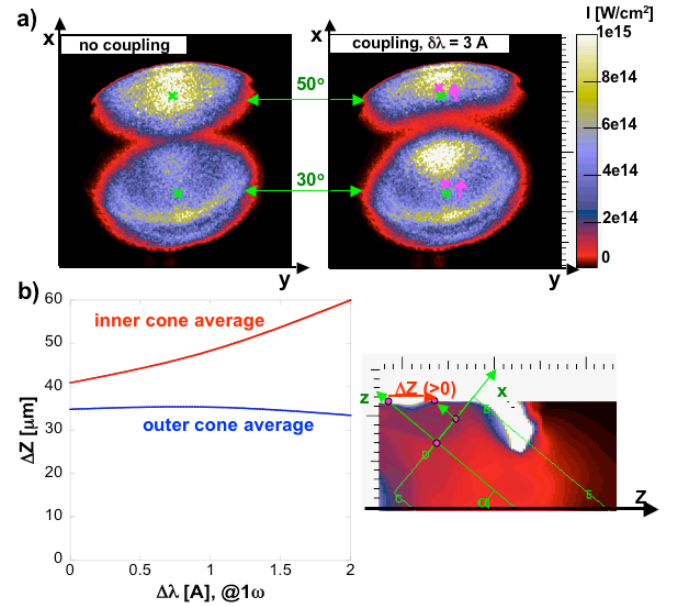


FIG. 8: a) Laser intensity in the transverse plane (x,y) at $z=2$ mm for the 30° and 50° beams, with coupling turned off (no transfer), and with coupling and $\delta\lambda=3$ Å. b) Shift of the intensity-weighted center of the inner and outer cones, measured as a shift ΔZ on the hohlraum wall ($\Delta Z > 0$ towards the LEH) from the center position without transfer.

Figure 8b shows the shift averaged over the inner and outer cones, defined as the shift on the hohlraum wall (>0 towards the LEH). It is interesting to see that the transfer leads to a systematic shift towards the LEH regardless of the wavelength shift, including at the 0.6 Å shift that cancels transfer between the cones. The reason is illustrated in Fig. 9. The transfer first occurs from the

inner towards the outer beam outside the LEH, and then from the outer towards the inner inside the LEH. Since the beams swap position at the LEH, it turns out that the beam transferring energy to the other is always the beam on top, which leads to a shift upwards (i.e. towards the LEH) in both cases. Even when the net transfer between the inner and outer cones is zero, at $\Delta\lambda=0.6\text{\AA}$, there is still some transfer occurring between some pairs of beams which contributes to the pointing shift. The shift is of the order of 30 to 50 microns on the hohlraum wall.

C. Comparison of several target designs

We have performed the same analysis for several target designs under consideration for NIF. No SSD bandwidth was included for this comparison. The three designs all have a Be ablator. Their features are summarized in Table II, and the curves of energy transfer vs. wavelength shift are plotted in Fig. 10 next to the hohlraum electron densities at peak laser power.

The first design, has the highest radiation temperature of the three, at 300 eV; laser intensities are also the highest, which makes it more sensitive to laser plasma instabilities but allows a lower total laser energy. The second design features a larger hohlraum with lower electron density and laser intensities, thus requiring more laser energy. The energy transfer values are lower than for the first design due to smaller densities and lower laser intensities (Fig. 10b).

The last design is a smaller design (subscale of the first by a factor 0.9) which is a candidate for the first energetics campaign on NIF in 2009. Unlike the other two, it is not designed to reach ignition, but to emulate the hohlraum conditions with less laser energy. The energy transfer is very similar to the first design despite lower laser intensities, due to the $\simeq 20\%$ lower temperature (T_e at the LEH is about 5.2 keV for the subscale design, vs.

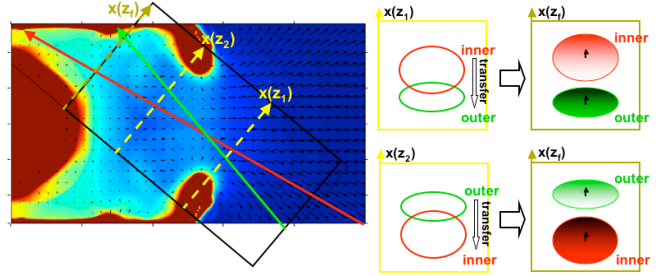


FIG. 9: Schematics of the effects of crossed-beam transfer on the effective beam pointing (here for the 30° , 50° pair): in each of the two transfer zones, the beam on top (inner beam outside the LEH, outer beam inside the LEH) always transfer to the beam on the bottom, leading to a systematic shift towards the LEH regardless of the overall transfer.

6.3 keV for the 300 eV target) and larger spot sizes for half of the beams, making the overlap slightly bigger (especially near the LEH where the coupling is maximum - cf. Fig. 5a).

Rad. temp.	Hohlraum / LEH \varnothing	23.5° beams I [W/cm ²] / spot scale	30° beams	44.5° beams	50° beams
300 eV	5.1 mm / 2.55 mm	$5.1 \cdot 10^{14}$ / 1	$5.1 \cdot 10^{14}$ / 1	$1.1 \cdot 10^{15}$ / 1	$1.1 \cdot 10^{15}$ / 1
285 eV	6 mm / 3 mm	$3.8 \cdot 10^{14}$ / 1.175	$3.8 \cdot 10^{14}$ / 1.175	$8.7 \cdot 10^{14}$ / 1.175	$8.7 \cdot 10^{14}$ / 1.175
285 eV	4.58 mm / 2.54 mm	$2.5 \cdot 10^{14}$ / 1.07	$2.9 \cdot 10^{14}$ / 1	$5.8 \cdot 10^{14}$ / 1.07	$6.6 \cdot 10^{14}$ / 1

TABLE II: Radiation temperature, hohlraum and LEH diameters, and intensity and spot size scale factor for the three target designs studied here. The 1.0 scale for the spot size corresponds to ellipse dimensions of $0.824 \times 0.59 \text{ mm}^2$ and $0.593 \times 0.343 \text{ mm}^2$ for the inner (23.5°, 30°) and outer (44.5°, 50°) beams, respectively. The other spot sizes are simply obtained by multiplying these dimensions by the scaling factor.

It is interesting to see that despite the differences in the slopes of the curves of energy transfer vs. $\Delta\lambda$, the wavelength shift that cancels the net transfer between the inner and outer cones is remarkably robust, around 0.4 - 0.5 Å. This is explained by the similarity of the beams geometry and flow orientation around the LEH; the range of wavelength shift available on NIF (from 0 to 3 Å) appears sufficient to control energy transfer in the forthcoming ignition experiments.

D. Symmetry analysis

The power transfer values obtained for each beam (at different $\delta\lambda$) were then examined with a 3-D view-factor code to determine the sensitivity of symmetry to a two-color separation. In this simulation the hohlraum/capsule albedo and laser conversion efficiency were tuned to reproduce radiation-hydrodynamics results, and to reproduce the correct symmetry optimum

at peak laser power. The results are shown in Fig. 11. As expected, the optimum symmetry occurs at ~ 0.6 Å, where the net transfer between the inner and outer cones balances to zero (Fig. 7b). At $\delta\lambda$ above or below this value asymmetry is increased, primarily in Legendre mode 2, since the principal effect of the two-color scheme is to redistribute power between the inner and outer cone similar to a cone balance adjustment. This suggests symmetry may be tuned using a two-color scheme if the margin for cone balance adjustment is limited (i.e. if the laser is power limited on one cone) [25].

The $\simeq 0.5\%$ asymmetry level at $\delta\lambda=0.6$ Å is acceptable at peak power if averaged to less over the whole pulse.

The effects of the shift of the effective beam pointing observed in the previous section were investigated with similar view-factor analysis calculations. The same symmetry calculations were run with a fixed pointing shift of 35 and 45 μm towards the LEH for the outer and inner beams respectively, as previously indicated by Fig. 8. The main effect is a change of the second Legendre mode asymmetry (pole-waist) by about 0.1%. The effect on all other modes is even smaller, so the net effect on the total asymmetry is negligible.

We also determined the sensitivity of transfer and symmetry to the electron temperature. We arbitrarily increased by 50% the electron temperature at the LEH (the flow was also increased by $\sqrt{1.5}$ for consistency). Indeed, measurements in the LEH region have observed an

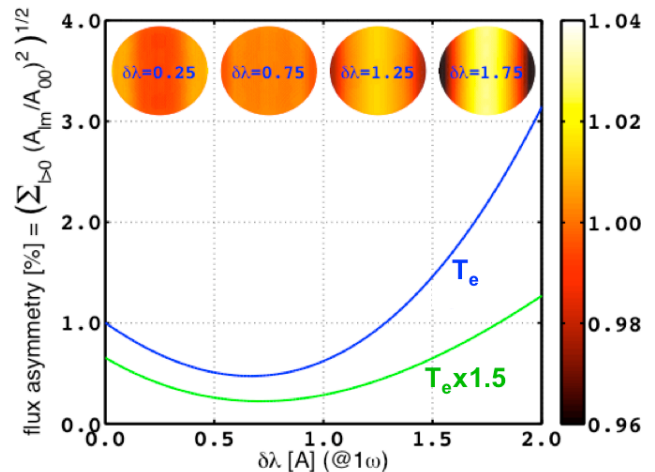


FIG. 11: Area-weighted flux asymmetry (defined as the r.m.s of the spherical harmonics A_{ij}) on the ignition capsule for the nominal electron temperature T_e at the LEH and for an arbitrary increase of T_e by 50%. The color maps on top show the x-ray flux on the capsule (the hohlraum axis is horizontal).

increase in T_e over the calculations [26], possibly due to magnetic fields. The transfer turns out to scale mainly as predicted by the fluid limit, i.e. like T_e^{-1} and as a function of $\delta\lambda/\sqrt{T_e}$. The optimum $\delta\lambda$ is indeed shifted towards higher wavelengths if T_e is increased, as observed in Fig. 11. However, the transfer and hence the asymmetry are also reduced, which should preserve a good symmetry even if the temperature is higher than predicted.

V. CONCLUSION

In summary, we have performed the first comprehensive 3D modeling of the crossed beam power transfer for ignition experiments, with realistic laser and plasma conditions. The long interaction lengths and large powers at ignition scale lead to energy transfer despite being out of resonance. The coupling appears to be linear (small gain limit), and is therefore easily scalable to other designs. Optical smoothing techniques effects have been analyzed; polarization smoothing is expected to reduce the transfer by a factor two, whereas smoothing by spectral dispersion may increase it if the bandwidth is large enough to include significant contributions from the resonance peaks. Tuning the frequency shift between the laser beams is expected to allow a control of the power balance between the inner and outer cones on NIF and to maintain a good implosion symmetry.

Acknowledgments

This work was performed under the auspices of the U.S. Department of Energy by Lawrence Livermore Na-

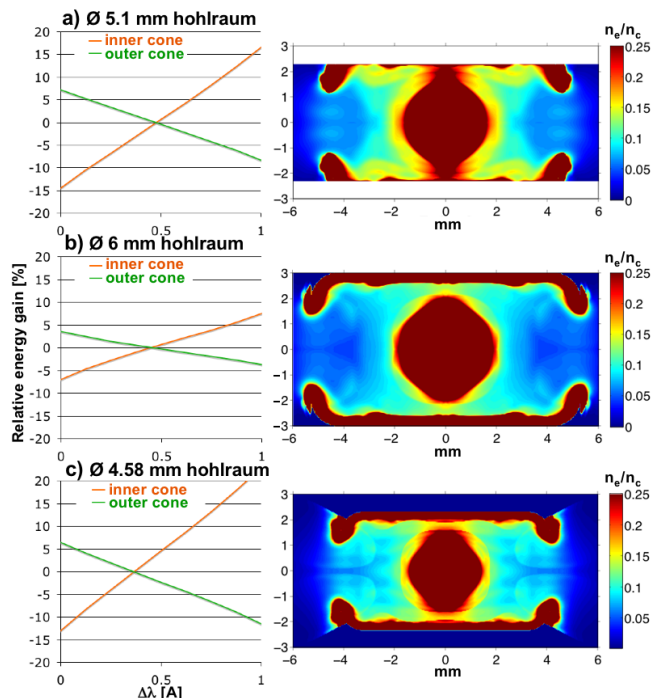


FIG. 10: Relative energy transfer between the inner and outer cones for three ignition target designs (cf. Table II); the electron density maps of the designs at peak laser power are shown on the right.

tional Laboratory under Contract DE-AC52-07NA27344.

-
- [1] J. Lindl et al., Phys. Plasmas **11**, 339 (2004).
 - [2] S. H. Glenzer et al., Nature Physics **3**, 716 (2007).
 - [3] P. A. Hohlstein et al., Nuclear Fusion **44**, S177 (2004).
 - [4] N. Fleurot, C. Cavailler, and J. L. Bourgade, Fusion Engineering and Design **74**, 147 (2005).
 - [5] W. L. Kruer et al., Phys. Plasmas **3**, 382 (1996).
 - [6] V. V. Eliseev, W. Rozmus, V. T. Tikhonchuk, and C. E. Capjack, Phys. Plasmas **6**, 3 (1996).
 - [7] C. J. McKinstrie, J. S. Liu, R. E. Giacone, and H. X. Vu, Phys. Plasmas **7**, 3 (1996).
 - [8] R. K. Kirkwood et al., Phys. Rev. Lett. **76**, 2065 (1996).
 - [9] R. K. Kirkwood et al., Phys. Plasmas **4**, 1800 (1997).
 - [10] K. B. Wharton et al., Phys. Rev. Lett. **81**, 2248 (1998).
 - [11] K. B. Wharton et al., Phys. Plasmas **6**, 2144 (1999).
 - [12] R. K. Kirkwood et al., Phys. Rev. Lett. **89**, 215003 (2002).
 - [13] B. I. Cohen et al., Phys. Plasmas **5**, 3408 (1998).
 - [14] E. A. Williams et al., Phys. Plasmas **11**, 231 (2004).
 - [15] C. Labaune et al., Phys. Rev. Lett. **85**, 1658 (2000).
 - [16] H. A. Baldis et al., Phys. Rev. Lett. **77**, 2957 (1996).
 - [17] R. L. Berger et al., Phys. Plasmas **5**, 4337 (1998).
 - [18] J. F. Drake, P. K. Kaw, Y. C. Lee, G. Schmidt, C. S. Liu, and M. N. Rosenbluth, Phys. Fluids **17**, 778 (1974).
 - [19] G. B. Zimmerman and W. L. Kruer, Comments Plasma Phys. Control. Fusion **2**, 51 (1975).
 - [20] M. M. Marinak, G. D. Kerbel, N. A. Gentile, O. Jones, D. Munro, S. Pollaine, T. R. Dittrich, and S. W. Haan, Physics of Plasmas **8**, 2275 (2001).
 - [21] J. W. Goodman, *Introduction to Fourier optics* (McGraw-Hill Publishing Company, 1968).
 - [22] H. A. Rose and D. F. Dubois, Phys. Fluids **B 5**, 590 (1993).
 - [23] E. Lefebvre et al., Phys. Plasmas **5**, 2701 (1998).
 - [24] D. Froula et al., Phys. Rev. Lett. **101**, 115002 (2008).
 - [25] P. Michel et al., Phys. Rev. Lett. (2008), in press.
 - [26] S. H. Glenzer et al., Phys. Plasmas **6**, 2117 (1999).